ADVANCED MATERIALS
www.advmat.de

In-Operando Spatiotemporal Imaging of Coupled Film-Substrate Elastodynamics During an Insulator-to-Metal Transition

*Greg Stone, Yin Shi, Matthew Jerry, Vladimir Stoica, Hanjong Paik, Zhonghou Cai, Darrell G. Schlom, Roman Engel-Herbert, Suman Datta, Haidan Wen, Long-Qing Chen, and Venkatraman Gopalan**

The drive toward non-von Neumann device architectures has led to an intense focus on insulator-to-metal (IMT) and the converse metal-to-insulator (MIT) transitions. Studies of electric field-driven IMT in the prototypical VO_2 thin-film channel devices are largely focused on the electrical and elastic responses of the films, but the response of the corresponding TiO_2 substrate is often overlooked, since it is nominally expected to be electrically passive and elastically rigid. Here, in-operando spatiotemporal imaging of the coupled elastodynamics using X-ray diffraction microscopy of a VO_2 film channel device on TiO_2 substrate reveals two new surprises. First, the film channel bulges during the IMT, the opposite of the expected shrinking in the film undergoing IMT. Second, a microns thick proximal layer in the substrate also coherently bulges accompanying the IMT in the film, which is completely unexpected. Phase-field simulations of coupled IMT, oxygen vacancy electronic dynamics, and electronic carrier diffusion incorporating thermal and strain effects suggest that the observed elastodynamics can be explained by the known naturally occurring oxygen vacancies that rapidly ionize (and deionize) in concert with the IMT (MIT). Fast electrical-triggering of the IMT via ionizing defects and an active "IMT-like" substrate layer are critical aspects to consider in device applications.

1. Introduction

The drive for smaller, low-power, and different computing architectures has led to the search for a new generation of electronic materials that possess a controllable, fast electronic phase transition with several orders of magnitude change in conductivity. Materials exhibiting an insulator-to-metal transition (IMT), and conversely a metal-to-insulator transition (MIT), have demonstrated sub-picosecond intrinsic switching times in pump-probe measurements.[1–3] Device architectures using these materials have been proposed and demonstrated for next-generation electronic and neuromorphic computing.[4–7] Despite these successes, key questions remain as to whether the fast switching of the electronic state can be driven solely by the application and removal of an applied voltage.

Numerous attempts to answer this question exist in literature with considerable emphasis on VO_2[4,8–11,12] due to its strain tunable IMT temperature that occurs near

G. Stone, Y. Shi, M. Jerry, V. Stoica, L.-Q. Chen, V. Gopalan
Department of Materials Science and Engineering and Electrical Engineering
Pennsylvania State University
University Park
Pennsylvania 16802, USA
E-mail: vgopalan@psu.edu

H. Paik, D. G. Schlom
Department of Materials Science and Engineering
Cornell University
Ithaca, NY 14853, USA

Z. Cai
Advanced Photon Source
Argonne National Laboratory
Lemont, IL 60439, USA

R. Engel-Herbert
Paul-Drude-Institut für Festkörperelektronik
Leibniz-Institut im Forschungsverbund Berlin e.V
Hausvogteiplatz 5, 10117 Berlin, Germany

S. Datta
School of Electrical and Computer Engineering
Georgia Institute of Technology
Atlanta, GA 30332, USA

H. Wen
Materials Science Division and Advanced Photon Source
Argonne National Laboratory
Lemont, IL 60439, USA

The ORCID identification number(s) for the author(s) of this article can be found under https://doi.org/10.1002/adma.202312673

DOI: 10.1002/adma.202312673

room temperature and exhibits up to five orders of magnitude change in the magnitude of the electrical conductivity. To date, these efforts have demonstrated Joule heating,[13,14] changes in the material stoichiometry,[15–19] or the creation of defects[20–22] and lattice disordering[23] as mechanisms driving the IMT; however, demonstrating pure electronic control of the IMT has proven to be elusive. Investigations into the electronic control of the IMT show that Joule heating is the primary mechanism that causes the phase change. Often overlooked in these electronically driven IMTs is the role of defects and stoichiometry, except for liquid ionic gating experiments where extrinsic oxygen vacancy defects are actively injected into and out of the VO_2.[15–19] In two- and three-terminal device architectures employed in modern electronics, the electrodes are solid-state metals (instead of ionic liquids), and such interface electrochemistry leading to active defect injection is absent. Nonetheless, native oxygen vacancies are still present in these films as well as their substrates, and their concentration is known to have a large impact on the phase transitions in these materials.[15,24–27] However, it remains unknown as to what role these vacancies and their ionization and deionization dynamics play during the IMT. Further, the role of the substrate is largely overlooked, though as we will show, it indeed plays an active role both electrically and elastically in the IMT switching.

To better understand the dynamics of an electrically driven IMT in VO_2, we have performed the in-operando spatiotemporal mapping of the structure in a two-terminal device using a pulsed nanoscale X-ray probe. VO_2 was chosen for these studies due to its well-known phases and the ability to manipulate the IMT temperature via strain.[15,28] A number of recent in-operando studies have shed important light on the operation of a two-terminal device, including ultrafast electron diffraction,[29] in-operando electron microscopy,[30,31] optical reflectivity microscopy,[13] X-ray florescence and diffraction microscopy,[21,22] and X-ray-diffraction studies under ionic gating.[18] The spatiotemporal X-ray measurements made here differ from previous in-operando studies in three important aspects. First, unlike electron microscopy techniques[30,31,29] that require electron-transparent samples, the present study is performed on a bulk device in its native state requiring no modification of the film. Second, this work was done on single-crystal films avoiding grain boundary defects inherently present in polycrystalline films in prior studies.[21,22,32] Finally, the present study simultaneously probes both the dynamics of the film and deep inside the substrate (estimated as up to ≈14 μm in depth) unlike a prior study that probed ≈2–3 nm depth of the substrate.[33] The in-operando studies here demonstrate a complex structural transition in VO_2 from the insulating M_1 to the metallic R phase on a time scale longer than the change in conductivity in an electrically-driven IMT. Additionally, the elastic changes are contrary to what is expected in bulk VO_2 phases, indicating the role of point defects. We bring together vacancy electronic dynamics, diffusion, thermal, and strain effects into a unified macroscopic phase-field model for the operation of a VO_2 two-terminal device. It reveals a transition from neutral to ionized oxygen vacancies at the onset of the IMT that is strongly coupled to both the electronic and elastic changes across the IMT in VO_2 as well as in the TiO_2 substrate.

2. In-operando Spatiotemporal Diffraction Microscopy

The geometry of the two-terminal VO_2 devices is shown in **Figure 1a**. In the bulk state, VO_2 possesses an IMT at 340 K and undergoes a structural transition from a monoclinic M_1 (insulating) to a tetragonal/rutile R (metallic) phase. The IMT can also be driven through strain, doping, and defects, which can stabilize new crystal structures such as monoclinic M_2 and M_3, and tetragonal T phases.[34,35] For this study, 10 nm thin VO_2 single crystal films were grown on TiO_2 (001) substrates by molecular beam epitaxy, which were then processed into a series of 2-terminal devices using standard lithography techniques as described in the Experimental Section. The in-plane lattice mismatch between the metallic rutile VO_2 and the TiO_2 substrate results in a ≈0.85% epitaxial tensile strain in the VO_2 film, which lowers the IMT temperature to a measured 290 K (Figure S1, Supporting Information). The detailed device geometry is depicted in Figure S2 (Supporting Information).

Time-resolved X-ray diffraction (XRD) imaging measurements of the VO_2 transformation dynamics from the insulating M_1 to the metallic R state across the two-terminal were performed at the Advanced Photon Source (APS) at Argonne National Laboratory on the 2-ID-D beamline (Experimental Method and Figure 1a). The measured duration of the IMT was 1.5 μs (Figure 1b). The dynamics of the structural evolution of the VO_2 channel across the IMT was probed by measuring the position of the VO_2 M_1 $(40\bar{2})$ peak in reciprocal space at 0.5 μs time intervals. The mosaics of diffraction intensity distributions were post-processed to calculate the changes in the reciprocal space mean location (Δq_x and $\Delta q_{y,z}$) and the variance [$\sigma(q_{y,z})$], of the diffracted X-rays (Figure 1c). During the off-state (electrically insulating M_1) the 2D maps of Δq_x and $\Delta q_{y,z}$ show high uniformity across the 2-terminal device channel and under the electrodes. This drastically changes at the onset of the IMT (0 μs delay) where strong local changes in Δq_x and $\Delta q_{y,z}$ are observed; the Δq_x is across the 10 μm width of the device while $\Delta q_{y,z}$ is across the 6 μm length of the device. Subsequent time delay measurements show that the changes to Δq_x and $\Delta q_{y,z}$ reach a maximum at a 1 μs delay before gradually relaxing over the next 5 μs back toward a uniform distribution. Interestingly, this structural evolution occurs over a much longer time scale than the observed electronic transition ≈1 μs. The sign changes in Δq_x across the width of the channel and $\Delta q_{y,z}$ across the length of the channel indicate a bulge of the lattice planes as depicted in Figure 1d. This bulge is surprising since the transformation to the metallic R phase should lead to a shrinkage of the lattice parameter out-of-plane as measured in equilibrium lattice parameter changes (Figure S3, Supporting Information). Another surprising observation is that a similar mapping with the substrate Bragg peaks shows that TiO_2 (002) also coherently bulges in a similar manner (Figure S4, Supporting Information). We look at these surprising aspects more closely next and tie them to ionizing oxygen vacancies concurrent with the IMT.

Figure 2a shows the projections of the constructed reciprocal space maps (RSMs) into the q_y,q_z plane for three different points (P_1, P_2, and P_3) across the 6 μm length of the 2-terminal device for time delays of "off," 0, 1, and 6 μs. The change in intensity at each of the points and the time delays from the "off" state

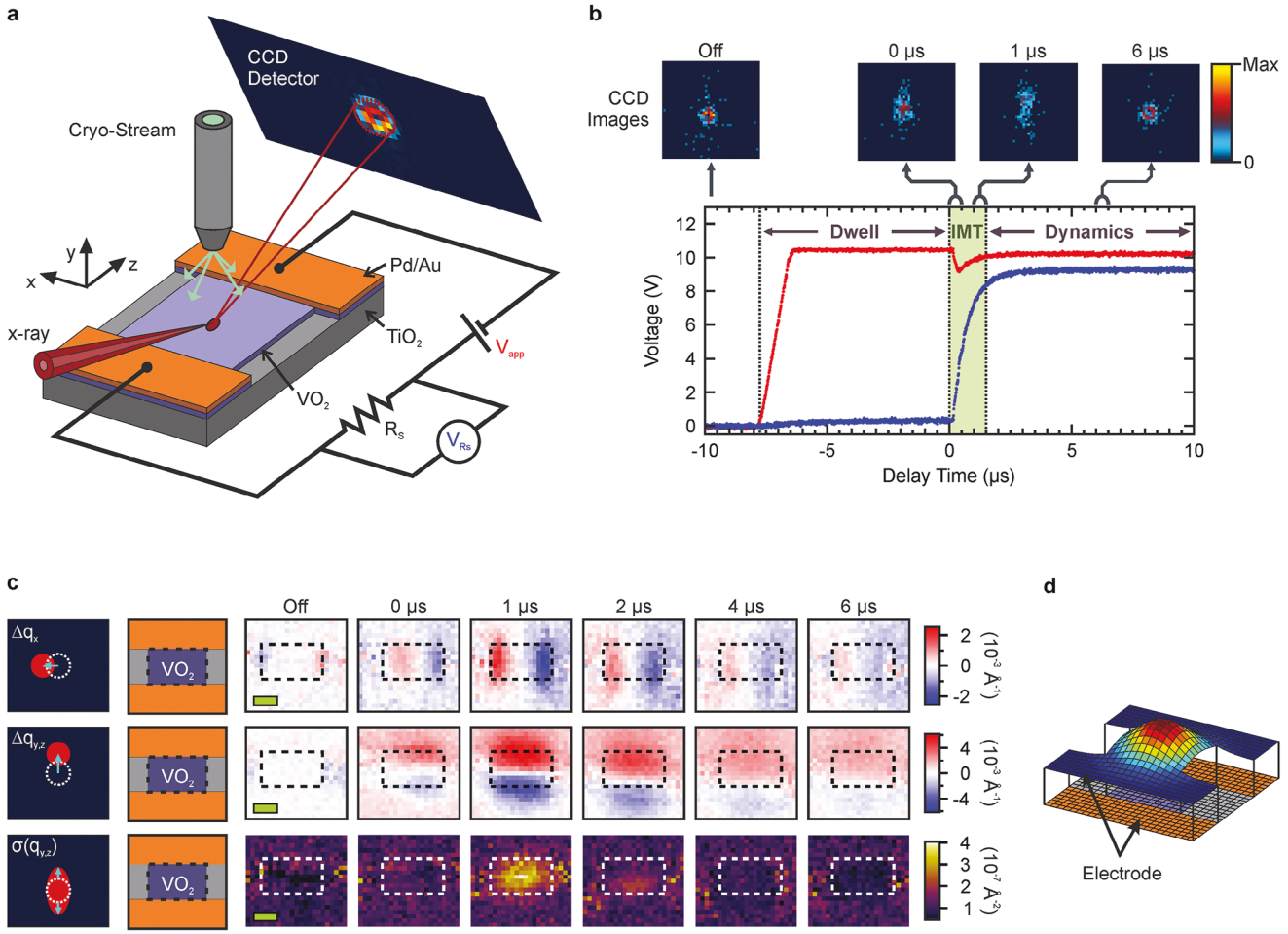

Figure 1. a) Schematic of the in-operando synchrotron X-ray imaging setup at the beamline. A simple circuit of the two-terminal VO_2 device is connected in series to a function generator and a resistor, of which the voltage drop across (V_{Rs}) is used to monitor the electrical state of the VO_2 device. The two-terminal device is mounted onto a 3-axis stage and placed into a focused X-ray beam. The temperature of the device was maintained at 245 K by a flow of cold nitrogen gas. The diffracted X-rays are captured on a Pilatus 100 K area detector. b) Voltage versus time of the applied voltage pulse (red curve) and voltage drop across the series resistor (blue curve). A ≈7 µs dwell time is observed before the onset of the IMT (green region) and confirms that the two-terminal device starts in the "off" insulating state. Above the voltage versus time plot is the recorded diffraction intensity for four different time intervals from the insulating, IMT, and metallic phases. Large changes in the diffracted intensity distribution are shown during the IMT. c) Time-resolved shifts in the Bragg peak during the IMT [from $M_1(40\bar{2})$ to the R (002)] in the *x*-direction (Δq_x, first row) and in the *y*–*z* plane at an angle of ≈26° to the *y*-axis ($\Delta q_{y,z}$, second row) shows that the film in the channel transiently bulges in the middle (right schematic) within 1–2 µs following the IMT followed by a relaxation of the bulge on a longer time scale. The third row shows the broadening of the variance, $\sigma(q_{y,z})$, indicating that the broadening of the Bragg peak is the largest during the IMT transition (green window in panel b). d) A schematic of the lattice distortion across the VO_2 channel deduced from the imaging in panel c.

are shown in Figure S5 (Supporting Information). The RSMs for the remaining time delays are shown in Figure S6 (Supporting Information). During the "off" state, a well-resolved single peak corresponding to the insulating VO_2 M_1 $(40\bar{2})$ peak is observed. At the onset, 0 µs delay of the electrically driven IMT, this single peak splits into two distinct peaks. The first peak (α) shows a decrease in q_y by −0.024 Å^{-1} (or −0.53%), which corresponds to an increase in the out-of-plane lattice spacing of the VO_2 film, consistent with the bulge in Figure 1d. The direction of this shift is opposite to what is expected for the metallic R peak in VO_2, which has a shorter out-of-plane lattice spacing than M_1 (Figure S3, Supporting Information). The other peaks shift positive (γ) or negative (β) in q_z ±0.009 Å^{-1}, which corresponds to a rotation about the *x*-axis by ≈0.1°, depending on its location across the lengths (*z*-position in Figure 1a) of the sample. Neither of these peaks is located at the position of the VO_2 R (002) Bragg peak, which has a smaller out-of-plane lattice (larger q_y) than the VO_2 M_1 peak corresponding to a q_y value larger than the M_1 $(40\bar{2})$ position (Figure S3, Supporting Information). Tracking the position of these peaks as a function of time delay (Figure 2b) shows that the three peaks migrate toward the VO_2 R peak location and become indistinguishable at a time delay of ≈2–3 µs. Afterward, the peaks continue to gradually move toward the VO_2 R (002) Bragg peak but have yet to stabilize at the 6 µs delay mark despite the electrical transition finishing over 4.5 µs earlier (1.5 µs delay).

To examine the spatial behavior of these peaks across the 6 µm channel length of the 2-terminal device, $\theta/2\theta$ and rocking curves

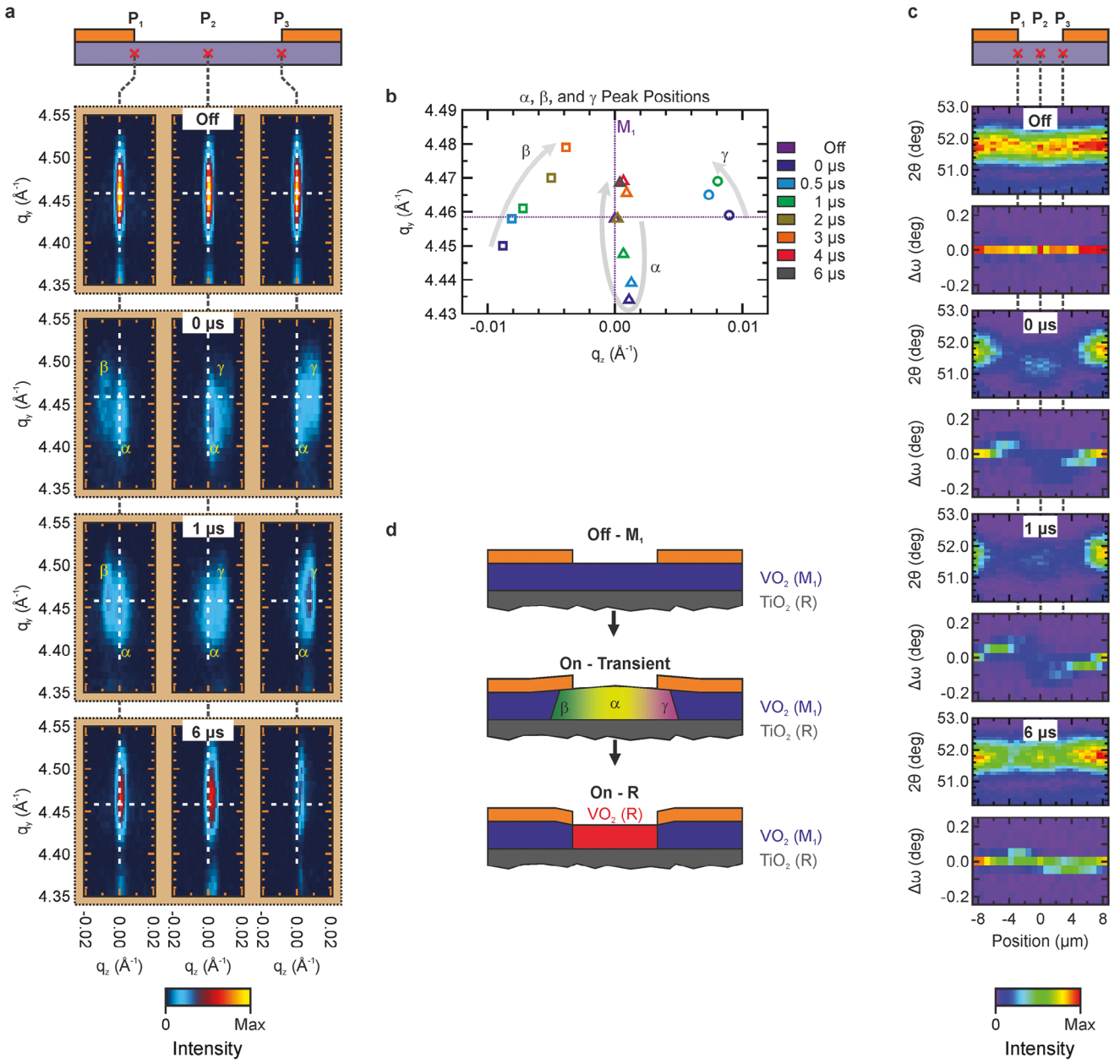

Figure 2. Dynamics of the VO_2 M_1 $(40\bar{2})$ peak across the IMT: a) Projection of the reconstructed 3D reciprocal space map in the (q_y,q_z) plane for three different VO_2 channel positions ($P_1 = -3$ µm, $P_2 = 0$ µm, and $P_3 = 3$ µm) and four different time delays ("off", 0, 1, and 6 µs). The centroid of the monoclinic M_1 peak is indicated by the white dashed lines. At the onset of the IMT (0 µs) the VO_2 M_1 peak splits into two peaks at three distinct positions in reciprocal space labeled α, β, and γ. b) Plot of the average centroid positions in q_y and q_z of the α, β, and γ peaks for the different time delays showing a gradual migration toward the VO_2 R (002) position on a time scale longer than the 1.5 µs observed for the electronic transition. c) $\theta/2\theta$ and rocking curves ($\Delta\omega$) of a 1D spatial line scan across the two-terminal device at the four time delays shown in panel a. As illustrated in the RSM, there is a decrease in the 2θ value at the onset of the IMT, which is in the opposite direction of the VO_2 R (002) peak. Note the θ /2θ and rocking curve traces the vertical and horizontal dashed lines, respectively, in panel a. d) An illustration (not to scale) showing additional VO_2 domains emerging at the onset of the IMT not found in either the M_1 or R equilibrium states that give rise to the observed α, β, and γ peaks.

about the VO_2 M_1 $(40\bar{2})$ peak were collected at 0.75 µm steps, which respectively follow the vertical and horizontal dashed lines shown in Figure 2a. Figure 2c shows the results for the time delays "off," 0, 1, and 6 µs, with the remainder of the time delays shown in Figure S6 (Supporting Information). For the "off" state, both the $\theta/2\theta$ and the rocking curves show a uniform film of the M_1 VO_2. At the start (0 µs) of the IMT, there is a uniform shift in intensity to a lower 2θ value across the center 4 µm stretch of the device channel length, while the transition region from the channel to the electrodes shows a large decrease in intensity. Concurrently, there is a large decrease in the rocking curve intensity across the center of the device, while at the electrode

transition region, the intensity shifts to a higher or lower rocking angle depending on the position. These measurements are again consistent with the swelling of the out-of-plane lattice parameter in VO_2 within the channel region seen in Figures 1 and 2. Additionally, the α, β, and γ peaks observed in the RSMs in Figure 2a are uniform across a region of several micrometers. As with the RSM measurements, the changes in the $\theta/2\theta$ and rocking curve maps migrate over the next 6 µs to the expected VO_2 R (002) peak but have yet to achieve equilibrium at 6 µs.

Figure 2d shows a conceptual illustration of the evolution of the VO_2 structure due to the voltage-initiated IMT derived from the X-ray data. In the "off" state, there is a uniform film of the VO_2 M_1 phase both under the electrodes and within the channel. At the onset of the IMT, the VO_2 undergoes a growth of the out-of-plane lattice parameter (α); however, the VO_2 under the electrodes is still M_1. This necessitates transition regions (β and γ) with crystal planes rotated in opposite directions to maintain the continuity of the crystal planes between the swollen VO_2 within the channel and the nominal M_1 phase under the electrodes. Over time, the swelling decreases and the VO_2 within the channel becomes metallic R with a small transition region. Phase-field modeling discussed further on suggests that this swelling spatially correlates with a gradient in the *ionized* oxygen vacancy concentration in the film from the center (α peak) toward the sides (β,γ peaks) of the channel closer to the electrodes.

Next, we look at the elastodynamics of the TiO_2 substrate. **Figure 3a** shows the constructed projection of the RSM in the q_y-q_z plane for the TiO_2 (002) Bragg peak for the time delays "off", 0, 1, and 6 µs. Also shown are the data for five spatial positions across the 2-terminal device, P_0 through P_4, with P_1, P_2, and P_3 corresponding to the same positions for VO_2 in Figure 2a. The RSM projections for the other time delays and additional spatial locations are shown in Figure S7 (Supporting Information). In the "off" state, the q_y,q_z projections for each of the spatial positions across the 2-terminal device show an intensity distribution that is consistent with the bulk TiO_2 (002) peak. At the onset of the IMT (0 µs delay), a large amount of diffracted intensity is observed in the q_y,q_z projections at lower q_y values in both the positive and the negative q_z values. This scattered intensity outside the bulk Bragg peak shall henceforth be referred to as the "tail." The total diffracted intensity in the tail can be more than twice that in the bulk (002) peak (Figure 3b); hence ≈2/3rd of the penetration depth of the X-rays (≈14 µm) yields an estimate of ≈9–10 µm of the TiO_2 substrate near the surface that has undergone a structural change. At its most extreme, the tail intensity extends -0.024 Å^{-1} (or -0.55%) in q_y and 0.01 Å^{-1} in q_z from the center of the bulk TiO_2 (002) peak. In comparison, the bulk Bragg peak has a width of 0.008 Å^{-1} in q_y and 0.003 Å^{-1} in q_z when measured at the 1% intensity of its maximum. The shape of the tail's intensity distribution is not simply an elongation of the Bragg rod in q_y, as would be expected for a uniform thin region. Instead, it curves from $+q_z$ to $-q_z$ as it propagates lower in q_y. This distribution indicates that the focused X-ray beam is simultaneously probing many different discrete out-of-plane lattice spacings and tilts. As the delay time increases, the size of the tail in the q_y,q_z projection quickly decreases over the first 2 to 3 µs and then slowly converges back to the bulk Bragg intensity distribution. Like the VO_2 film, the remnant of the tail gradually decreases past ≈2 µs and is still observed at the 6 µs time delay. Oversampling due to the spread of the incident wavevectors in the focused beam was ruled out as the sole cause of the intensity outside the bulk substrate peak of (002), by placing a virtual slit on the CCD to reduce the impact of the spread of incident wavevectors; while the amount of intensity outside the bulk substrate peak drops, there is still a significant amount of intensity compared to the bulk peak. The origin instead is likely related to the dynamical scattering from the modified TiO_2 layer, which is sensitive to crystal disorder and can enhance the scattering intensities.[36,37]

3. Phase-Field Modeling and Discussion

In conjunction with the results observed in the VO_2 film, a clearer picture emerges on what is occurring within the region surrounding the 2-terminal device. Both the TiO_2 substrate and the VO_2 film experience a large swelling at the onset of the IMT (Figure 3c). As a result, the VO_2 film is lifted and bowed into a dome shape leading to modification of the strain within the VO_2 film. This creates domains within the VO_2 film with different crystal structures, which are reminiscent of those observed in bent VO_2 nanobeams.[38,39] To get a better understanding of how such transient swelling can be introduced via electric fields, we present a phase-field model to describe how oxygen vacancy dynamics could be crucial to the swelling of the VO_2 film. A phase-field model incorporating both the electronic[40] and structural effects of oxygen vacancies, is developed to understand the origins of the transient elastic deformations observed by the X-ray during the electronically driven IMT (see Experimental Section and Supporting Information for the model details). We use this model to simulate the phase transition of the VO_2 thin film in the electrode/VO_2/TiO_2 system supplied with a periodically pulsing voltage. Snapshots of various fields are shown in **Figure 4**.

We begin by noting that $[V_O^{tot}] = [V_O^{\cdot\cdot}] + [V_O^{\times}]$, where $[V_O^{\times}]$ is the concentration of the neutral oxygen vacancies. At equilibrium ("off" state), the concentration of the total oxygen vacancies $[V_O^{tot}]$ in the substrate (≈0.0077 f.u.$^{-1}$) is approximately an order of magnitude less than that in the film (≈0.044 f.u.$^{-1}$) (Figure 4d). This is due to the much higher oxygen vacancy formation energy of the TiO_2 than that of VO_2 (Supporting Information). The defect level of oxygen vacancies is located near the midpoint of the energy gap of VO_2 so that the ionized oxygen vacancies $V_O^{\cdot\cdot}$ constitute only ≈10% of the total oxygen vacancies V_O^{tot} in the insulating M_1 state (Figure 4c).

After the voltage is turned on, the film is Joule heated and an increasing number of itinerant electrons and holes are generated; however, the VO_2 film initially remains in the insulating M_1 phase. After a 5.9 µs incubation period, the temperature of the film reaches the IMT temperature of 338 K (Figure S8, Supporting Information) and abruptly begins to transform into the metallic R phase. We note that the simulated IMT temperature more closely represents the bulk VO_2 IMT temperature than what is observed in the grown film (290 K), which is likely due to the plane strain approximation (zero strain perpendicular to the cross-section, which underestimates the strain effect) used in the simulations; a 3D strain distribution indeed predicts a decrease in the transition temperature.[41] At the onset of the IMT (relabeled 0 µs), there is an abrupt decrease in the structural order parameter η (Figure 4e) and the electronic band gap E_g (Figure 4f) in the VO_2 film to values between the insulating M_1 and

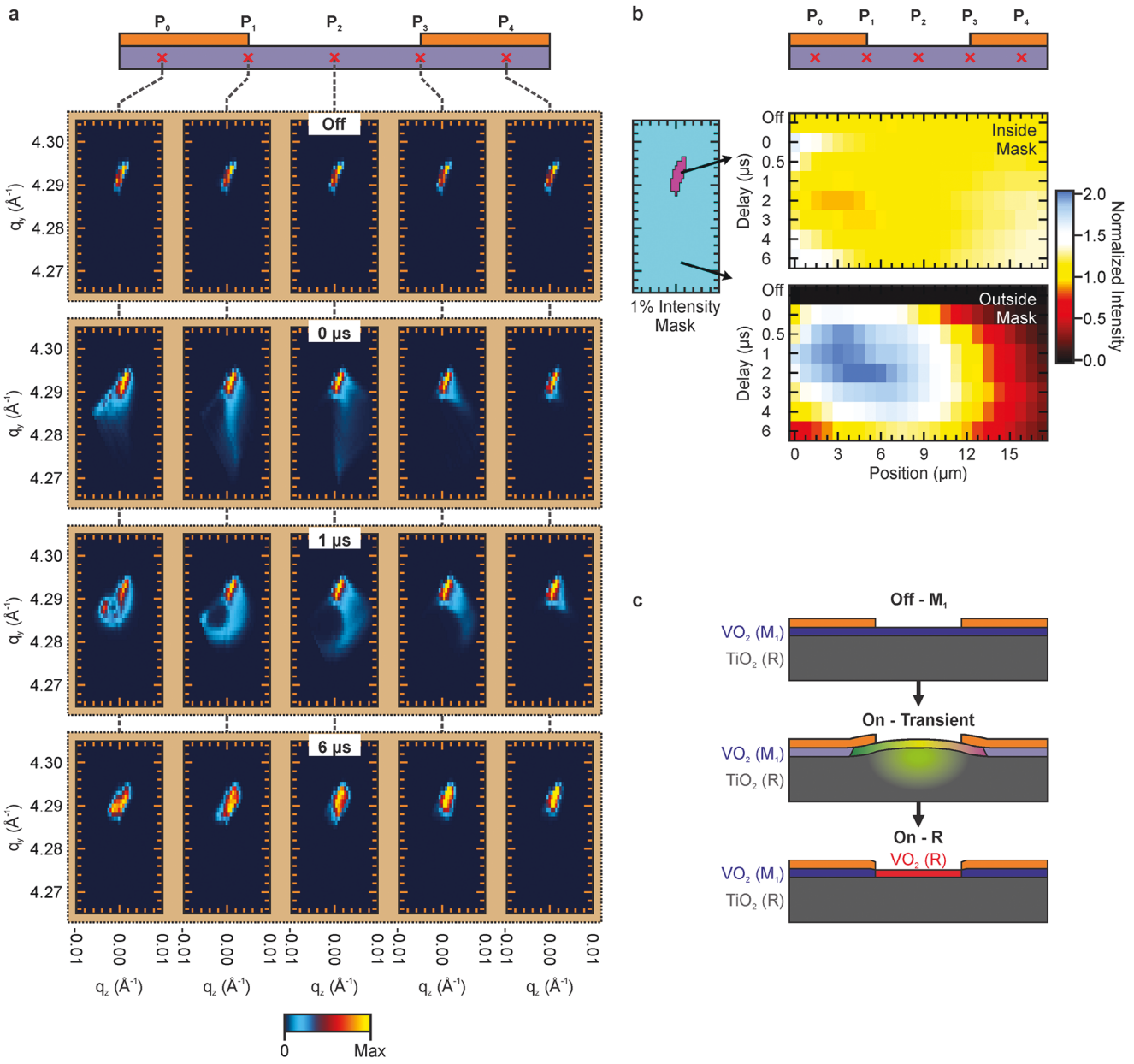

Figure 3. Dynamics of the TiO_2 R (002) peak across the IMT: a) Projection of the reconstructed 3D RSM in the plane of the TiO_2 (002) Bragg peak for five different positions (P_0, P_1, P_2, P_3, and P_4) along the VO_2 channel in the two-terminal device. The RSM is shown for four different time delays (off, 0, 1, and 6 µs), with the intensity distribution shown at "off" corresponding to the bulk TiO_2 R (002) Bragg peak. At the onset of the IMT (0 µs), a large increase in intensity outside the Bragg peak emerges sweeping to lower q_y, whose profile in reciprocal space is dependent both on the time delay and spatial position. Remnants of this intensity outside the Bragg rod are visible out to 6 µs, with a time-scale evolution remnant of what was observed in the VO_2 M_1 peak. b) Plot of the normalized integrated XRD intensity of the TiO_2 (002) Bragg rod across the 2-terminal devices at different time delays above a similar plot of the integrated intensity outside the bulk TiO_2 (002) Bragg rod. The integration mask used to construct the plots is shown on the left. A large increase in scattered X-ray intension outside the Bragg rod along with an increase in the total diffracted X-ray intensity is observed. c) An illustration (not to scale) of the expansion of the substrate giving rise to the long tails in the Bragg peak. Included is the domain structure in the VO_2 film.

metallic R phase, which indicates that the VO_2 film has taken on an intermediate transient phase. Concurrently, almost all the neutral oxygen vacancies in the film ionize, that is, $V_O^{\times} \rightarrow V_O^{\cdot\cdot} + 2e'$ (Figure 4c), because the defect level is now in the conduction band (Figure S9, Supporting Information) due to the band gap reduction. The free electrons suddenly released from the oxygen vacancies promote the IMT by screening the electron–electron Coulomb interaction.[42,43] While the neutral oxygen vacancies are ionizing, there is no net movement of the vacancies into or out of the VO_2 film (Figure 4d) due to their slow diffusion. Importantly, the out-of-plane (Figure 4a) and rotation/shear (Figure 4b) strain in the VO_2 channel increases abruptly, consistent with the

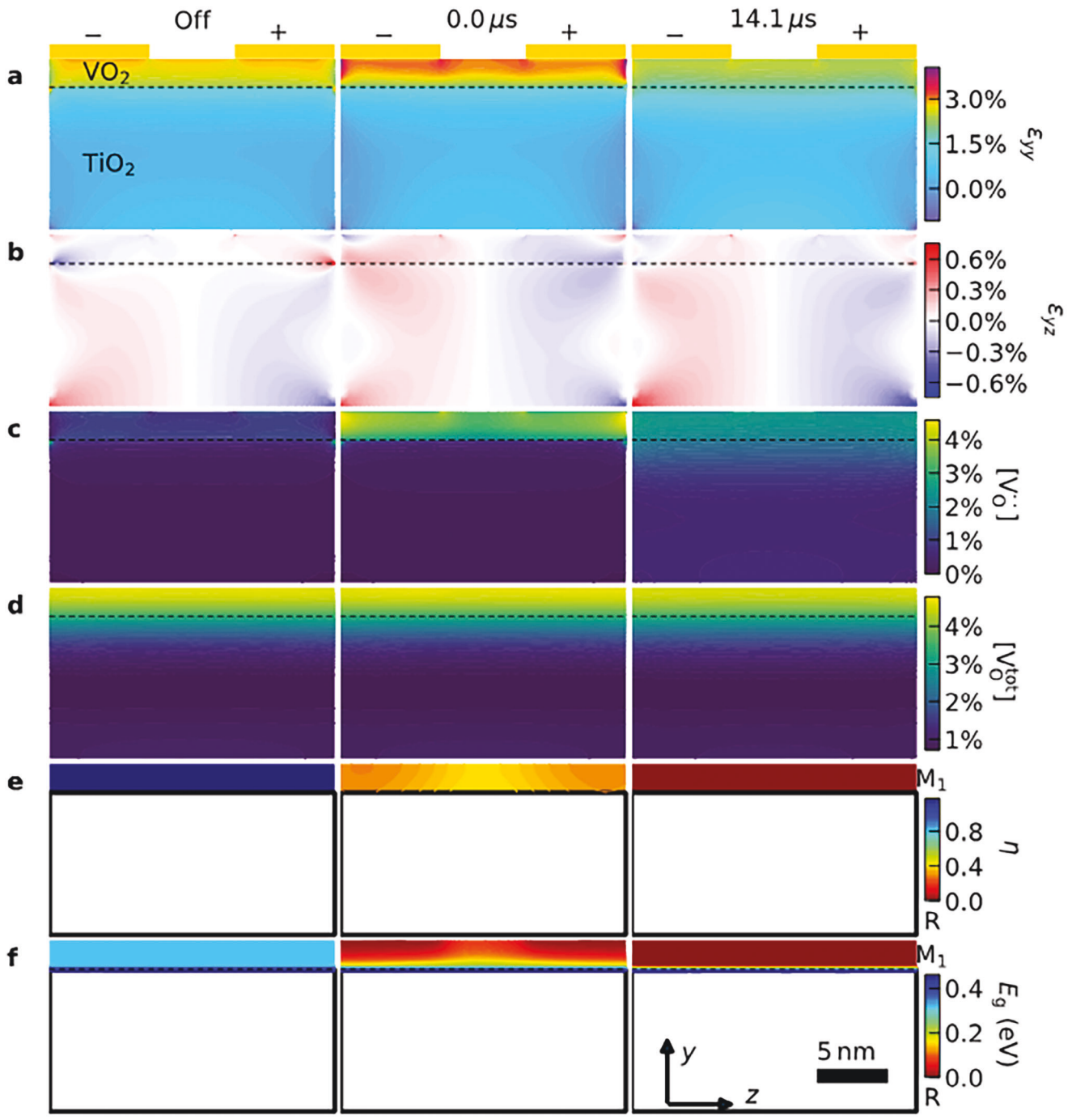

Figure 4. Phase-field simulation of the voltage-induced IMT in VO_2/TiO_2 system with oxygen vacancies. Snapshots of the *y*–*z* planar cross-section (in Figure 1b) at three different time delays, namely, off-state, 0 μs (onset of the IMT), and 14.1 μs are shown. The dashed lines indicate the interface between the VO_2 film and the TiO_2 substrate. The gold bars on top of the panel a represent the electrodes whose polarity is marked by the minus and plus signs. The scale bar and coordinate system are displayed at the corner of panel f) Panel a) Out-of-plane strain, ϵ_{yy}; panel b) Shear strain in the cross-section plane, ϵ_{yz}; panel c) the concentration of the *ionized* oxygen vacancies $[V_O^{\cdot\cdot}]$ in units of per formula unit; panel d) the *total* concentration of both ionized and neutral oxygen vacancies $[V_O^{tot}] = [V_O^{\cdot\cdot}] + [V_O^{\times}]$ in units of per formula unit; panel e) the structural order parameter η in the VO_2 film ranging from the R ($\eta = 0$) to M_1 ($\eta \approx 1$) phases; panel f) the electron energy gap in the VO_2 film, ranging from zero (metal) to 0.32 eV (insulator). The substrate is colored white in panels e) and f) as these order parameters are relevant only in the film region.

synchrotron X-ray data. This anomalous lattice expansion arises from the IMT-induced sudden ionization of oxygen vacancies, whose expanding defect strain in the ionized state is larger than that in the neutral state.[44,45] We have also simulated the same process in the absence of oxygen vacancies and have only seen a shrinkage of the VO_2 film in the out-of-plane direction (Figure S10, Supporting Information), as expected for the M_1-to-R structural phase transition.

After the IMT (14.1 µs), the ionized oxygen vacancies gradually recombine with the electrons injected from the electrode (Figure 4c), leading to a shrinkage of the out-of-plane lattice parameter until it reaches the equilibrium R-phase values (Figure 4a). To confirm that the shrinkage arises from the electron injection, we also simulate the thermally triggered IMT with zero voltage, showing that after the IMT, the ionized oxygen vacancies remain ionized and the bulge persists (Figure S11, Supporting Information). The concentration of ionized oxygen vacancies in the TiO_2 substrate near the interface increases due to diffusion from the VO_2 film and local thermal excitation, resulting in an expansion of the out-of-plane lattice parameter there (Figure 4a). In the experiment, however, the swelling of the substrate occurs at the onset of the IMT, possibly because the band gap of TiO_2 near the interface could also be changing due to its proximity to the VO_2 film, and oxygen vacancies there also suddenly ionize as the gap closes. This possible effect is not considered in the phase-field model (Figure S9, Supporting Information) since it causes difficulty for convergence in the current computational implementation. The model does indicate a lattice expansion of both the film and the substrate due to oxygen vacancy ionization as seen in the experiments. This discovered mechanism indicates that the transient swelling of the VO_2 film and substrate should be ubiquitous for any oxide substrate satisfying two conditions: 1) The defect level of oxygen vacancies in the substrate is deep enough in the band gap in the insulating state so that the vacancies are mostly neutral, and 2) The substrate undergoes an IMT-like transition in proximity to the VO_2 film so that the vacancies there ionize as the gap closes. The physics of this proximity effect, by which a microns thick surface layer of VO_2 also exhibits IMT-like behavior is presently not understood, and hence not considered in the phase-field modeling; it is an exciting avenue to pursue in future studies.

4. Conclusion

In summary, we reveal an exquisitely detailed electro–chemo–thermo–mechanical mechanism underlying the IMT transition in a 2-terminal VO_2 film device on a TiO_2 substrate. In-operando electrical voltage cycles repeatedly trigger the IMT in the VO_2 film channel, which is spatiotemporally imaged using XRD microscopy. It reveals new transient changes to the crystal structure not observed in equilibrium, strain dynamics upon the IMT that is different from purely thermally driven phase transitions, and surprisingly, dramatic strain in the TiO_2 substrate that also appears to develop an IMT-like layer microns deep. The realization of the missing link, that two types of vacancies exist, one neutral and the other ionized, and that the latter has a larger defect strain than the former, results in a transient expansion of the lattice parameter (rather than a contraction as would be expected in equilibrium) when the IMT results in the ionization of the neutral vacancies. The ionization state–strain coupling of the oxygen vacancies during the IMT and the active electrical and elastic roles of the substrate with an "IMT-like" microns-thick layer closely coupled to the IMT in the film are new fundamental insights gleaned from this study that should inform device design. The positive feedback process due to vacancy ionization is predicted to shorten the IMT time,[40] which then leads to Mott electronic oscillators exhibiting higher frequencies desired for neuromorphic engineering.

5. Experimental Section

5.0.0.1. VO_2 Film Synthesis and Characterization: Ultrathin 10 nm VO_2 was grown on TiO_2 (001) substrates by reactive oxide molecular-beam epitaxy using a Veeco GEN10 system. The 0.9% lattice mismatch between the room temperature VO_2 R phase and the TiO_2 substrate resulted in commensurate VO_2 films with a shortened out-of-plane spacing. 2-terminal devices that were 10 µm in width by 6 µm in length were fabricated using standard lithographic techniques. Electrical contacts were patterned on the VO_2 surface using electron beam lithography to create a 20 nm-thick Pd/80 nm-thick Au metal stack in the defined patterns by electron beam evaporation, followed by lift-off. The active channel and device isolation were then patterned by electron beam lithography followed by a CF_4 dry etch and residual e-beam resist was stripped with a 70 °C bath of Remover 1165. Finally, the sample was mounted on a ceramic package and device electrodes were wire-bonded to external leads.

5.0.0.2. X-Ray Diffraction Microscopy: A sample with multiple 2-terminal devices was mounted onto a computer-controlled 3-axis stage and connected to a simple circuit with a series resistor to facilitate monitoring of the electric state of the VO_2 channel. The voltage applied across the circuit was low enough to allow for a dwell time before the onset of the IMT to ensure the device returned to the insulating state after each voltage pulse. The experiments conducted on the 2-ID-D beamline at APS were performed using a pulsed 10.1 keV hard X-ray beam, with a pulse duration of 100 ps and pulse spacing of 153 ns. The beam was focused down to a sub-micron probe (250 nm spot size) using an Au Fresnel lens (1.6 µm thick, 160 µm diameter, 100 nm outer zone width, and 40 µm center disk) in conjunction with a 20 µm diameter order sorting aperture. The sample temperature was maintained by a flowing nitrogen gas with a controlled temperature over the sample. To collect sufficient XRD intensity of the 10 nm VO_2 films for 0.5 µs time steps across the IMT, the experiment operated in a stroboscopic mode with thousands of exposures constituting a single time delay measurement. The VO_2 M_1 $(40\bar{2})$ peak position was measured along the center of the 10 µm device width for a series of time delays ("off", 0, 0.5, 1, 2, 3, 4, and 6 µs) between the X-ray pulse and the onset of the IMT to monitor the structural evolution. The time delay series was chosen to monitor the structural response of the film during and after the electrical changes associated with the IMT.

The diffracted X-ray intensity was captured using a Pilatus 100 K detector with a pixel pitch of 172 um and a size of 487 pixels by 195 pixels. The dynamic range of the detector was set to 20 bits. The detector was placed 0.837 m from the sample, giving the acceptance angle of 0.012° (or 0.21 mrad). The Pilatus was set to integrate 0.5 µs intervals at different time delays with respect to the voltage drop across the series resistor monitored by an oscilloscope. A stroboscopic measurement of ≈10 kHz triggering events was performed for each time delay to build up enough signal intensity to reach desired signal-to-noise ratios. It was estimated that over the duration of the full experiment, the device underwent over 10 million switching cycles. Spatial maps of the diffracted intensity were collected by spatially scanning the sample through the X-ray probe using computer-controlled stages. The step size for each of the spatial maps was set to 750 nm or 3× the width of the probe spot size. Each of the spatial scans were performed for fixed $\theta/2\theta$ angles. Once the spatial scans were completed the $\theta/2\theta$ angle was adjusted and the spatial scan was repeated. $\theta/2\theta$ step sizes of 0.05/0.1 degrees and 0.005/0.01 degrees were done for VO_2 and TiO_2, respectively. The VO_2 saw a larger $\theta/2\theta$ step, sized to cap-

ture the full-intensity distribution along q_y orientation due to its 10 nm thickness. Much finer step sizes in the TiO_2 substrate were used to observe subtle changes in the highly confined Bragg rod. Analysis of the 3D data sets (position z, $\theta/2\theta$ or position x, time delay, Pilatus x, Pilatus y) was done using a set of custom-written MatLab codes. The MatLab codes first calculated the scattering vector for each pixel within the Pilatus, which was then mapped to a reciprocal space vector. This was done for each of the $\theta/2\theta$ angles within a scan and allowed for the recorded diffraction intensity to be mapped to a particular location within reciprocal space. Using the series of $\theta/2\theta$ positions a full 3D reciprocal space maps of the VO_2 M_1 $(40\bar{2})$, VO_2 R (002), and TiO_2 (002) Bragg peaks were constructed. Analysis of the two peaks observed in the VO_2 RSM observed was done by simultaneously fitting two 2D Gaussian profiles, from which the center position of each fitted peak was extracted. Custom MatLab codes were then used to create a picture of the statics of the intensity distribution to create a picture of the spatial and temporal evolution of the VO_2 films and substrates in a readily readable manner.

While limited X-ray beamtime and signal-to-noise issues with some peaks prevented additional measurements in this study, future spatially resolved measurements across the phase transition in thermal equilibrium could clarify the difference with the electric field-driven IMT. The change of (40 $\bar{2}$) and (102) peak intensities in the M1 phase with spatial resolution could shed light on the vanadium dimers during the phase transition. Due to the large integration times required for the VO_2 film to acquire a good signal-to-noise ratio (S/N) to interpret the VO_2 data and resolve the peak splitting, only three locations, $P_{1\text{-}3}$ were collected in Figure 2; more locations could be collected in the future.

5.0.0.3. Phase-Field Modeling: The estimation of the time of the temperature increase over $\Delta T = 253$ K was first explained. A simple situation capturing the essential features of the experimental setup was considered: a $L_x = 10$ µm long (along the electric field), $L_y = 6$ µm wide, and $L_z = 10$ µm thick VO_2 sample was actively cooled by liquid nitrogen only through its top surface. Adopting the convection heat transfer coefficient of liquid nitrogen to be $h = 5 \times 10^4$ $Wm^{-2}K^{-1}$, the time for this temperature increase using the heat equation and Newton's law of cooling could be estimated,[29] $\Delta t = -(L_z C_v/h)\ln[1 - hL_xL_y\Delta T/(UI)] = 108$ µs, where C_v is the heat capacity per unit volume (see Supporting Information), and $U = 0.9$ V and $I = 5.1$ mA are respectively the voltage and current in the metallic phase. Here the macroscopic model is briefly introduced while the detail of the model is described in Supporting Information. The model is based on a previously established phase-field model of VO_2,[46–48] which employed a set of structural order parameters $\eta_i(\mathbf{r}, t)$ $(i = 1, 2, 3, 4)$ and a set of electronic order parameters $\psi_i(\mathbf{r}, t)$ $(i = 1, 2, 3, 4)$ to explicitly characterize the structural phases and the insulator/metal phases, respectively. Here $\mathbf{r}$ is the spatial coordinate and t is the time. The established model also includes the distribution of the free electrons $n(\mathbf{r}, t)$ and that of the free holes $p(\mathbf{r}, t)$ to describe the collective influence of the excess free carriers on the correlated electronic structure. Oxygen vacancies both in the film and the substrate were considered in this study. This was motivated both by the large changes in the variance of the Bragg peaks, the counter-intuitive out-of-plane expansion instead of contraction observed in both the film and the substrate, as well as previous studies that had indicated a key role of oxygen vacancies migrating in and out of VO_2 in modulating the lattice structure.[33,49–57,25,58,59] Unlike previous studies, the authors specifically consider two ionization states of the oxygen vacancies, the state losing two electrons $V_O^{\cdot\cdot}$ and the neutral state $V_O^{\times}$, and the defect strains $[V_O^{\cdot\cdot}]\Lambda$ and $[V_O^{\times}]\Lambda'$ generated by oxygen vacancies, which were assumed to be isotropic and volumetric. Here $[V_O^{\cdot\cdot}]$ and $[V_O^{\times}]$ are defect concentrations and Λ and Λ' were their respective compositional strain coefficients of oxygen vacancies. $\Lambda > \Lambda'$ was expected because of the greater Coulombic repulsion between an ionized oxygen vacancy and its neighboring cations as compared with the same interaction for a neutral oxygen vacancy. The dynamic chemical reactions between both types of oxygen vacancies and free electrons and holes were incorporated in the spatiotemporal evolution of the two types of oxygen vacancies. Such a complex and highly nonlinear system of partial differential equations was solved using the finite element method. To reduce the computational cost, a VO_2/TiO_2 system that was homogeneous in the x direction and model the temporal and spatial evolution of phases and oxygen vacancies as well as stress/strain and electric potential fields in the cross-section of the y–z plane was considered. A small cross-section consisting of a 2 nm thick VO_2 film, a 10 nm thick TiO_2 substrate, and two 1 nm thick gold electrodes was set up. The length of the film and substrate was set to 20 nm, and the length of the two electrodes was set to 7 nm. Appropriate boundary conditions were chosen, and all the assumed parameters are shown in Table S1 (Supporting Information).[24,44-47,60-65] While the simulation size of the device was much smaller than the actual device dimensions (10 nm thick and several micrometers long), it was found that the essential physical features observed in the experiments could be captured with this simulation system.

Supporting Information

Supporting Information is available from the Wiley Online Library or from the author.

Acknowledgements

G.S. and Y.S. contributed equally to this work. G.S., H.W., V.A.S., and V.G. acknowledge support for data collection, data analysis, and manuscript preparation from the DOE-BES grant DE-SC0012375. Y.S., L.-Q.C, and V.G. acknowledge the DOE-BES grant DE-SC0020145 for the development of the phase-field model and the simulations. H.W. acknowledges the support for designing the time-resolved XRD experiments from the DOE-BES, Materials Sciences and Engineering Division. This work made use of the synthesis facilities of the Platform for the Accelerated Realization, Analysis, and Discovery of Interface Materials (PARADIM), which were supported by the National Science Foundation under Cooperative Agreement No. DMR-2039380. The use of the Advanced Photon Source, a U.S. Department of Energy (DOE) Office of Science user facility operated for the DOE Office of Science by Argonne National Laboratory under Contract No. DE-AC02-06CH11357.

Conflict of Interest

The authors declare no conflict of interest.

Data Availability Statement

The data that support the findings of this study are available from the corresponding author upon reasonable request.

Keywords

Insulator-to-metal transition, phase-field modeling, TiO_2, VO_2, X-ray diffraction microscopy

Received: November 24, 2023
Revised: January 31, 2024
Published online: March 18, 2024

[1] A. Cavalleri, T. h. Dekorsy, H. H. W. Chong, J. C. Kieffer, R. W. Schoenlein, *Phys. Rev. B* **2004**, *70*, 161102.
[2] S. Lysenko, A. Rúa, V. Vikhnin, F. Fernández, H. Liu, *Phys. Rev. B* **2007**, *76*, 035104.
[3] L. A. Ladd, W. Paul, *Solid State Commun.* **1969**, *7*, 425.

[4] Z. Yang, C. Ko, S. Ramanathan, *Annu. Rev. Mater. Res.* **2011**, *41*, 337.
[5] S. Oh, Y. Shi, J. del Valle, P. Salev, Y. Lu, Z. Huang, Y. Kalcheim, I. K. Schuller, D. Kuzum, *Nat. Nanotechnol.* **2021**, *16*, 680.
[6] J. del Valle, J. G. Ramírez, M. J. Rozenberg, I. K. Schuller, *J. Appl. Phys.* **2018**, *124*, 211101.
[7] J. del Valle, P. Salev, Y. Kalcheim, I. K. Schuller, *Sci. Rep.* **2020**, *10*, 4292.
[8] K. Liu, S. Lee, S. Yang, O. Delaire, J. Wu, *Mater. Today Bio* **2018**, *21*, 875.
[9] Z. Shao, X. Cao, H. Luo, P. Jin, *npg Asia Mater.* **2018**, *10*, 581.
[10] R. Shi, N. Shen, J. Wang, W. Wang, A. Amini, N. Wang, C. Cheng, *Appl. Phys. Rev.* **2019**, *6*, 011312.
[11] Y. Ke, S. Wang, G. Liu, M. Li, T. J. White, Y. Long, *Small* **2018**, *14*, 1802025.
[12] M. Brahlek, L. Zhang, J. Lapano, H.-T. Zhang, R. Engel-Herbert, N. Shukla, S. Datta, H. Paik, D. G. Schlom, *MRS Commun.* **2017**, *7*, 27
[13] J. del Valle, N. M. Vargas, R. Rocco, P. Salev, Y. Kalcheim, P. N. Lapa, C. Adda, M.-H. Lee, P. Y. Wang, L. Fratino, M. J. Rozenberg, I. K. Schuller, *Science* **2021**, *373*, 907.
[14] H. Wen, L. Guo, E. Barnes, J. H. Lee, D. A. Walko, R. D. Schaller, J. A. Moyer, R. Misra, Y. Li, E. M. Dufresne, D. G. Schlom, V. Gopalan, J. W. Freeland, *Phys. Rev. B* **2013**, *88*, 165424.
[15] K. L. Gurunatha, S. Sathasivam, J. Li, M. Portnoi, I. P. Parkin, I. Papakonstantinou, *Adv. Funct. Mater.* **2020**, *30*, 2005311.
[16] J. Jeong, N. Aetukuri, T. Graf, T. D. Schladt, M. G. Samant, S. S. P. Parkin, *Science* **2013**, *339*, 1402.
[17] D. Passarello, S. G. Altendorf, J. Jeong, C. Rettner, N. Arellano, T. Topuria, M. G. Samant, S. S. P. Parkin, *Nano Lett.* **2017**, *17*, 2796.
[18] J. Jeong, N. B. Aetukuri, D. Passarello, S. D. Conradson, M. G. Samant, S. S. P. Parkin, *Proc. Natl. Acad. Sci. U. S. A.* **2015**, *112*, 1013.
[19] T. D. Schladt, T. Graf, N. B. Aetukuri, M. Li, A. Fantini, X. Jiang, M. G. Samant, S. S. P. Parkin, *ACS Nano* **2013**, *7*, 8074.
[20] Y. Kalcheim, A. Camjayi, J. del Valle, P. Salev, M. Rozenberg, I. K. Schuller, *Nat. Commun.* **2020**, *11*, 2985.
[21] A. G. Shabalin, J. Valle, N. Hua, M. J. Cherukara, M. V. Holt, I. K. Schuller, O. G. Shpyrko, *Small* **2020**, *16*, 2005439.
[22] A. G. Shabalin, J. del Valle, A. Charnukha, N. Hua, M. V. Holt, D. N. Basov, I. K. Schuller, O. G. Shpyrko, *ACS Appl. Electron. Mater.* **2020**, *2*, 2357.
[23] G. A. de la Peña Muñoz, A. A. Correa, S. Yang, O. Delaire, Y. Huang, A. S. Johnson, T. Katayama, V. Krapivin, E. Pastor, D. A. Reis, S. Teitelbaum, L. Vidas, S. Wall, M. Trigo, *Nat. Phys.* **2023**, *19*, 1489.
[24] Q. Lu, C. Sohn, G. Hu, X. Gao, M. F. Chisholm, I. Kylänpää, J. T. Krogel, P. R. C. Kent, O. Heinonen, P. Ganesh, H. N. Lee, *Sci. Rep.* **2020**, *10*, 18554.
[25] H. Zhang, L. Guo, G. Stone, L. Zhang, Y. Zheng, E. Freeman, D. W. Keefer, S. Chaudhuri, H. Paik, J. A. Moyer, M. Barth, D. G. Schlom, J. V. Badding, S. Datta, V. Gopalan, R. Engel-Herbert, *Adv. Funct. Mater.* **2016**, *26*, 6612.
[26] G. Li, D. Xie, Z. Zhang, Q. Zhou, H. Zhong, H. Ni, J. Wang, E. Guo, M. He, C. Wang, G. Yang, K. Jin, C. Ge, *Adv. Funct. Mater.* **2022**, *32*, 2203074.
[27] G. Li, D. Xie, H. Zhong, Z. Zhang, X. Fu, Q. Zhou, Q. Li, H. Ni, J. Wang, E. Guo, M. He, C. Wang, G. Yang, K. Jin, C. Ge, *Nat. Commun.* **2022**, *13*, 1729.
[28] J. H. Park, J. M. Coy, T. S. Kasirga, C. Huang, Z. Fei, S. Hunter, D. H. Cobden, *Nature* **2013**, *500*, 431.
[29] A. Sood, X. Shen, Y. Shi, S. Kumar, S. J. Park, M. Zajac, Y. Sun, L.-Q. Chen, S. Ramanathan, X. Wang, W. C. Chueh, A. M. Lindenberg, *Science* **2021**, *373*, 352.
[30] S. Cheng, M.-H. Lee, X. Li, L. Fratino, F. Tesler, M.-G. Han, J. del Valle, R. C. Dynes, M. J. Rozenberg, I. K. Schuller, Y. Zhu, *Proc. Natl. Acad. Sci. U. S. A.* **2021**, *118*, e2013676118.
[31] S. Cheng, M.-H. Lee, R. Tran, Y. Shi, X. Li, H. Navarro, C. Adda, Q. Meng, L.-Q. Chen, R. C. Dynes, S. P. Ong, I. K. Schuller, Y. Zhu, *Proc. Natl. Acad. Sci. U. S. A.* **2021**, *118*, e2105895118.
[32] K. Okimura, J. Sakai, S. Ramanathan, *J. Appl. Phys.* **2010**, *107*, 063503.
[33] T. D. Schladt, T. Graf, N. B. Aetukuri, M. Li, A. Fantini, X. Jiang, M. G. Samant, S. S. P. Parkin, *ACS Nano* **2013**, *7*, 8074.
[34] J. P. Pouget, H. Launois, J. P. D'Haenens, P. Merenda, T. M. Rice, *Phys. Rev. Lett.* **1975**, *35*, 873.
[35] M. Marezio, D. B. McWhan, J. P. Remeika, P. D. Dernier, *Phys. Rev. B* **1972**, *5*, 2541.
[36] A. Fukuhara, Y. Takano, *J. Appl. Crystallogr.* **1980**, *13*, 391.
[37] T. Saka, *J. Appl. Crystallogr.* **2003**, *36*, 249.
[38] R. Shi, Y. Chen, X. Cai, Q. Lian, Z. Zhang, N. Shen, A. Amini, N. Wang, C. Cheng, *Nat. Commun.* **2021**, *12*, 4214.
[39] W. Fan, S. Huang, J. Cao, E. Ertekin, C. Barrett, D. R. Khanal, J. C. Grossman, J. Wu, *Phys. Rev. B* **2009**, *80*, 241105.
[40] Y. Shi, V. Gopalan, L.-Q. Chen, *Phys. Rev. B* **2023**, *107*, L201110.
[41] Y. Shi, F. Xue, L.-Q. Chen, *Europhys. Lett.* **2017**, *120*, 46003.
[42] Y. Shi, L.-Q. Chen, *Phys. Rev. Appl.* **2019**, *11*, 014059.
[43] D. Wegkamp, M. Herzog, L. Xian, M. Gatti, P. Cudazzo, C. L. McGahan, R. E. Marvel, R. F. Haglund, A. Rubio, M. Wolf, J. Stähler, *Phys. Rev. Lett.* **2014**, *113*, 216401.
[44] L. Chen, Y. Cui, S. Shi, B. Liu, H. Luo, Y. Gao, *RSC Adv.* **2016**, *6*, 86872.
[45] B. Magyari-Köpe, S. G. Park, H.-D. Lee, Y. Nishi, *J. Mater. Sci.* **2012**, *47*, 7498.
[46] Y. Shi, L.-Q. Chen, *Phys. Rev. Appl.* **2019**, *11*, 014059.
[47] Y. Shi, L.-Q. Chen, *Phys. Rev. Appl.* **2022**, *17*, 014042.
[48] Y. Shi, F. Xue, L.-Q. Chen, *Europhys Lett* **2017**, *120*, 46003.
[49] K. L. Gurunatha, S. Sathasivam, J. Li, M. Portnoi, I. P. Parkin, I. Papakonstantinou, *Adv. Funct. Mater.* **2020**, *30*, 2005311.
[50] J. Jeong, N. Aetukuri, T. Graf, T. D. Schladt, M. G. Samant, S. S. P. Parkin, *Science* **2013**, *339*, 1402.
[51] D. Passarello, S. G. Altendorf, J. Jeong, C. Rettner, N. Arellano, T. Topuria, M. G. Samant, S. S. P. Parkin, *Nano Lett.* **2017**, *17*, 2796.
[52] J. Jeong, N. B. Aetukuri, D. Passarello, S. D. Conradson, M. G. Samant, S. S. P. Parkin, *Proc. Natl. Acad. Sci. U. S. A.* **2015**, *112*, 1013.
[53] R. Wang, T. Katase, K. Fu, T. Zhai, J. Yang, Q. Wang, H. Ohta, N. Koch, S. Duhm, *Adv. Mater. Interfaces* **2018**, *5*, 1801033.
[54] Y. Sharma, J. Balachandran, C. Sohn, J. T. Krogel, P. Ganesh, L. Collins, A. V. Ievlev, Q. Li, X. Gao, N. Balke, O. S. Ovchinnikova, S. V. Kalinin, O. Heinonen, H. N. Lee, *ACS Nano* **2018**, *12*, 7159.
[55] D. Schrecongost, H.-T. Zhang, R. Engel-Herbert, C. Cen, *Appl. Phys. Lett.* **2022**, *120*, 081602.
[56] D. Schrecongost, M. Aziziha, H. Zhang, I. Tung, J. Tessmer, W. Dai, Q. Wang, R. Engel-Herbert, H. Wen, Y. N. Picard, C. Cen, *Adv. Funct. Mater.* **2019**, *29*, 1905585.
[57] D. Schrecongost, Y. Xiang, J. Chen, C. Ying, H.-T. Zhang, M. Yang, P. Gajurel, W. Dai, R. Engel-Herbert, C. Cen, *Nano Lett.* **2020**, *20*, 7760.
[58] G. Li, D. Xie, Z. Zhang, Q. Zhou, H. Zhong, H. Ni, J. Wang, E. Guo, M. He, C. Wang, G. Yang, K. Jin, C. Ge, *Adv. Funct. Mater.* **2022**, *32*, 2203074.
[59] G. Li, D. Xie, H. Zhong, Z. Zhang, X. Fu, Q. Zhou, Q. Li, H. Ni, J. Wang, E. Guo, M. He, C. Wang, G. Yang, K. Jin, C. Ge, *Nat. Commun.* **2022**, *13*, 1729.
[60] C. Miller, M. Triplett, J. Lammatao, J. Suh, D. Fu, J. Wu, D. Yu, *Phys. Rev. B* **2012**, *85*, 085111.
[61] Z. Zhang, J. Chen, Y. Guo, J. Robertson, *Microelectron. Eng.* **2019**, *216*, 111057.
[62] Y. Cui, B. Liu, L. Chen, H. Luo, Y. Gao, *AIP Adv.* **2016**, *6*, 105301.
[63] Y. Sharma, J. Balachandran, C. Sohn, J. T. Krogel, P. Ganesh, L. Collins, A. V. Ievlev, Q. Li, X. Gao, N. Balke, O. S. Ovchinnikova, S. V. Kalinin, O. Heinonen, H. N. Lee, *ACS Nano* **2018**, *12*, 7159.
[64] Y. Gu, J. Cao, J. Wu, L.-Q. Chen, *J. Appl. Phys.* **2010**, *108*, 083517.
[65] P. P. Boriskov, M. A. Belyaev, A. A. Velichko, *Russ. J. Phys. Chem. A* **2017**, *91*, 1064.